Electronic Supplementary Information for:

Distinguishing deposition, corrosion, and stripping of transient heterogeneous materials during molecular electrocatalysis

*David J. Sconyers and James D. Blakemore**

Department of Chemistry, University of Kansas
1567 Irving Hill Road, Lawrence, KS 66045

*To whom correspondence should be addressed: blakemore@ku.edu

Contents

Infrared Spectroscopy

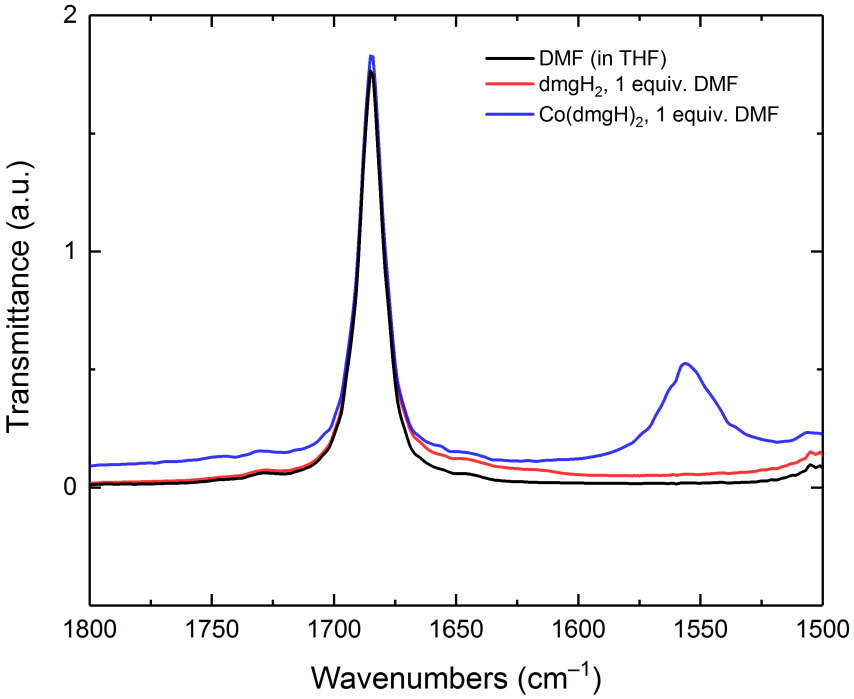

Figure S1. IR Spectra of the N-H stretch in $Co(dmgH)_2$. Spectra detailing the N-H stretch associated with the hydrogen evolution catalyst $Co(dmgH)_2$ (blue) in THF. The IR spectrum of dimethylformamide (black) and the free ligand $dmgH_2$ (red) are included for comparison, showing that the signal is unique to the synthesized, metal-containing complex.

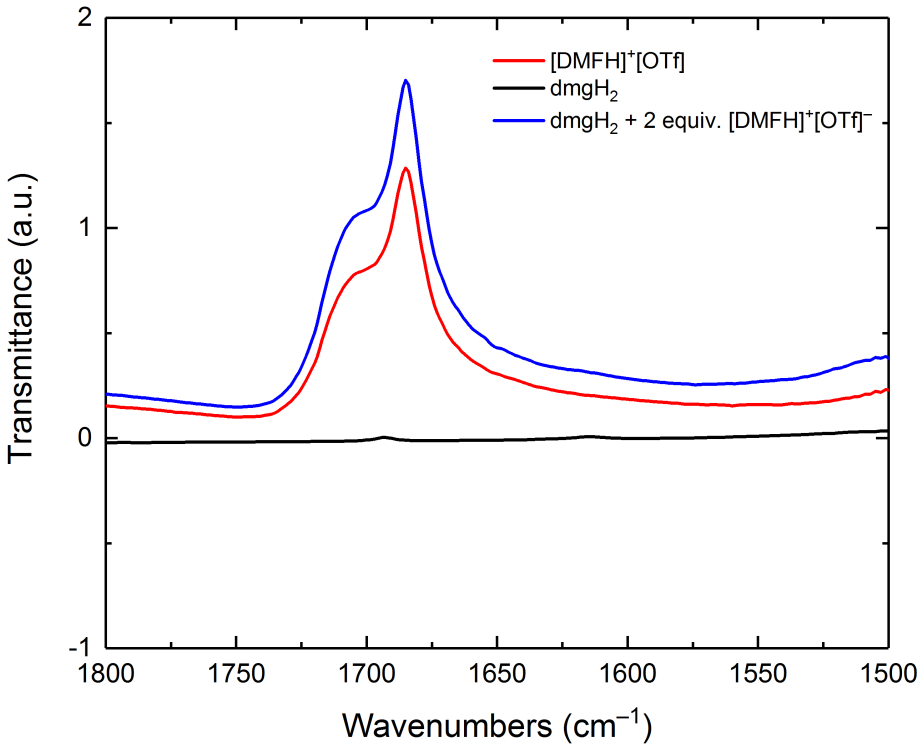

Figure S2. IR Spectra of $dmgH_2$ in the 1650 cm^{-1} region. IR spectra for free ligand $dmgH_2$ (black), $DMFH^+OTf^-$ (red) and $dmgH_2$ in the presence of the strong organic acid $DMFH^+$ (blue) in THF. As described in the main text, there is no signal intrinsic to free ligand, DMFH+ or a mixture of the two in the ~1650 cm^{-1} region.

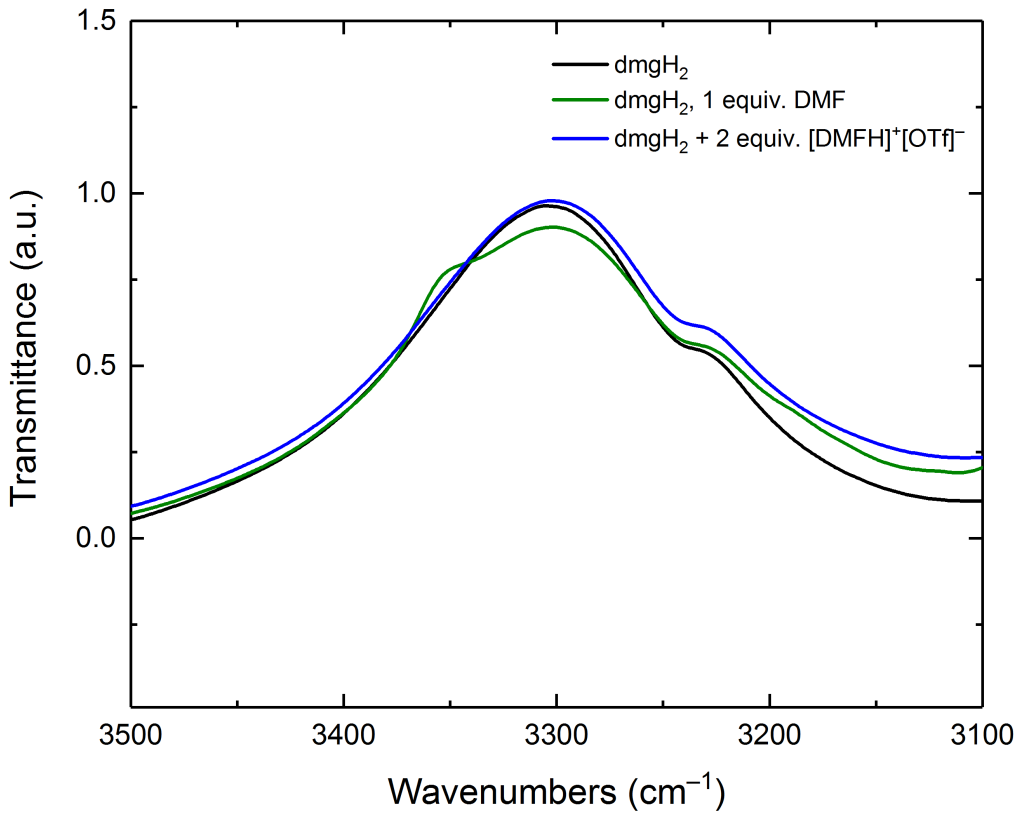

Figure S3. IR Spectra of dmgH$_2$ in the 3300 cm^{-1} region. IR spectra for free ligand dmgH$_2$ (black), dmgH$_2$ + DMF (green) and dmgH$_2$ in the presence of the strong organic acid DMFH$^+$ (blue) in THF. This region displays the O-H stretch associated with the free ligand, which is unperturbed in the presence of the acid used in these studies or its' conjugate base.

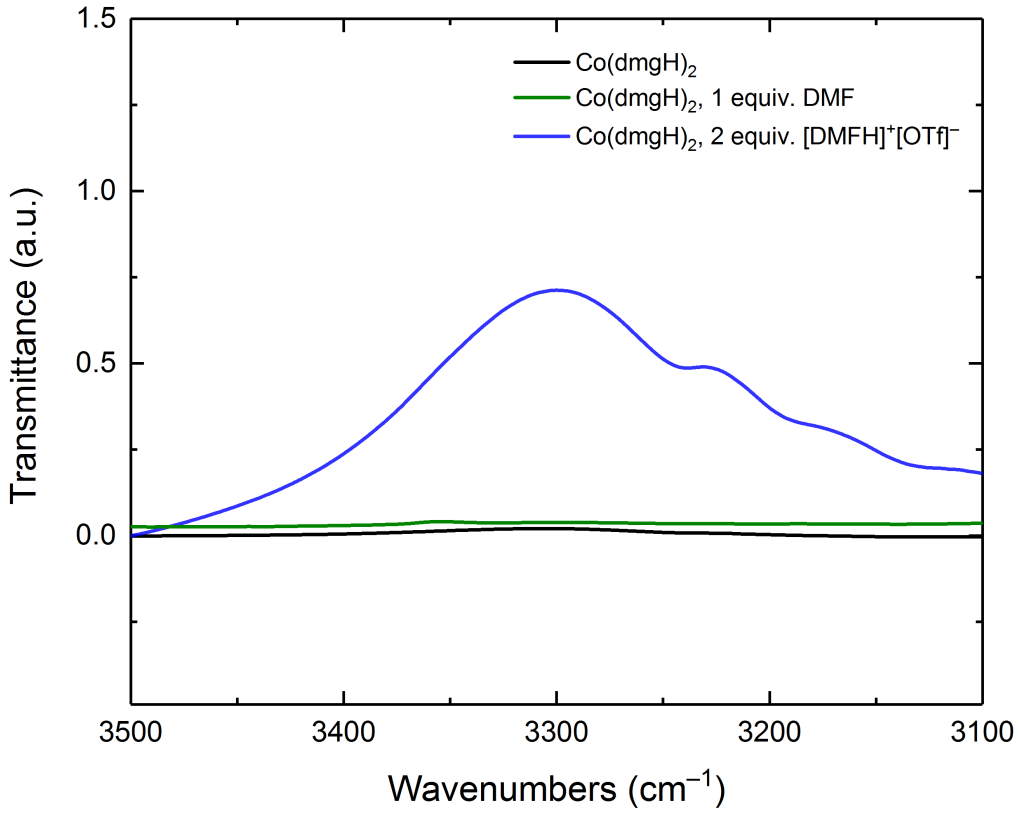

Figure S4. IR Spectra of Co(dmgH)$_2$ in the 3300 cm^{-1} region. IR spectra for the proton reduction catalyst Co(dmgH)$_2$ (black), Co(dmgH)$_2$ + DMF (green) and Co(dmgH)$_2$ + DMFH$^+$ (blue) in the 3300 cm^{-1} region in THF, where the O-H stretch for free ligand is expected. Note that the region is silent in the absence of added acid, and when the complex is treated with two equivalents of DMFH$^+$, it results in the generation of a signal similar to that of the free ligand dmgH$_2$.

UV-Visible Spectroscopy

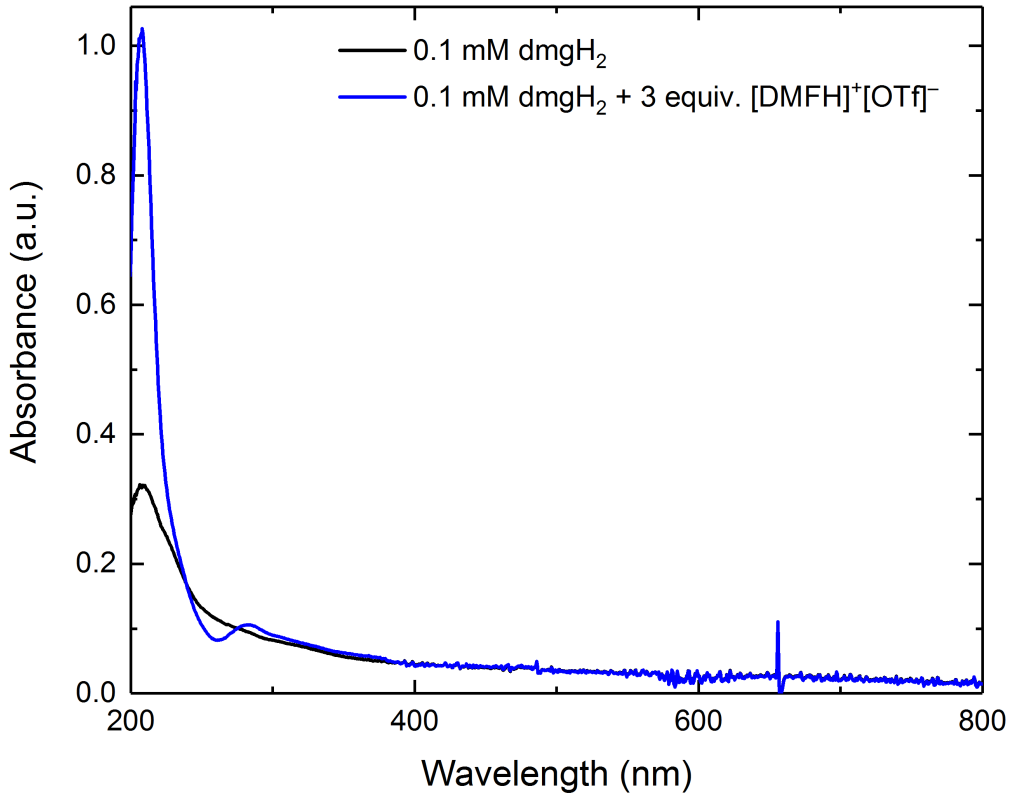

Figure S5. UV-Vis Spectra of the free ligand dmgH₂. UV-Visible spectra of the free ligand $dmgH_2$ (black) and $dmgH_2$ treated with three equivalents of the strong organic acid $DMFH^+$ (blue) in MeCN. As a common organic compound frequently used as a ligand, it has a single absorption in the UV region which can be attributed to $\pi \rightarrow \pi^*$ transitions, with the rest of the spectra silent. Addition of acid to the material results in minor changes in the absorption profile which result from overlapping absorptions between the free ligand and acid, but no generation of new signals.

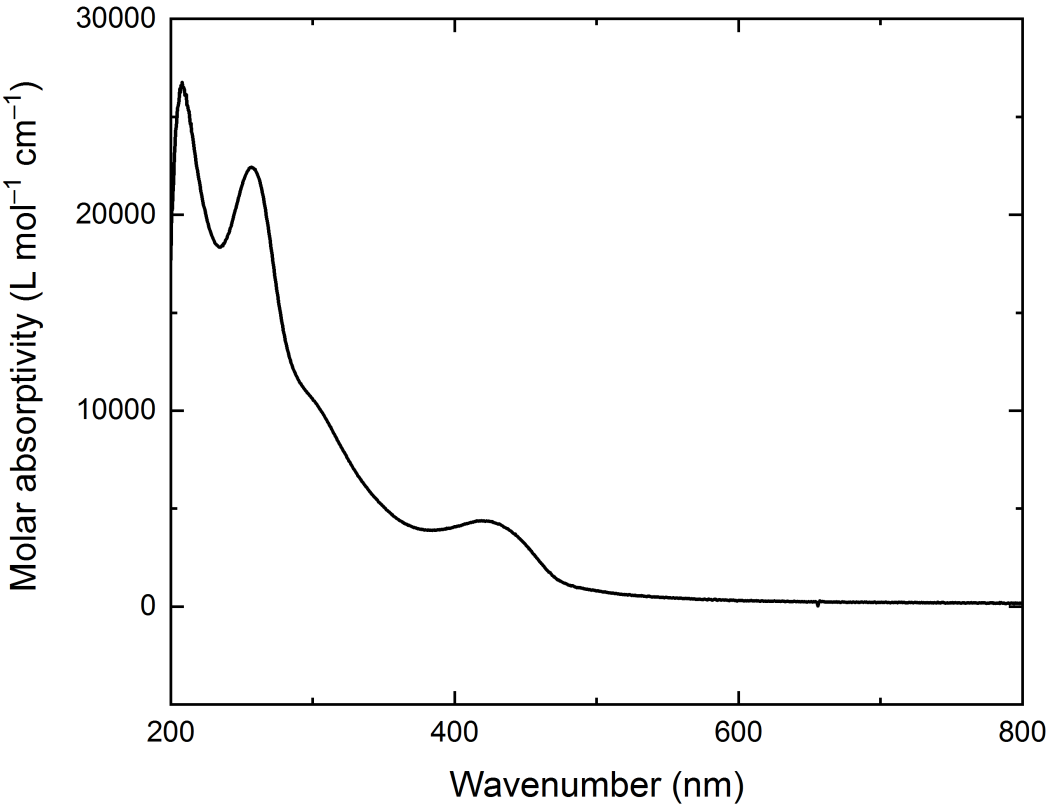

Figure S6. UV-Vis Spectra of Co(dmgH)$_2$. UV-Visible spectra of the complex Co(dmgH)2, exhibiting three absorptions bands with λ_{max} values of 257, 300, and 425 nm in MeCN.

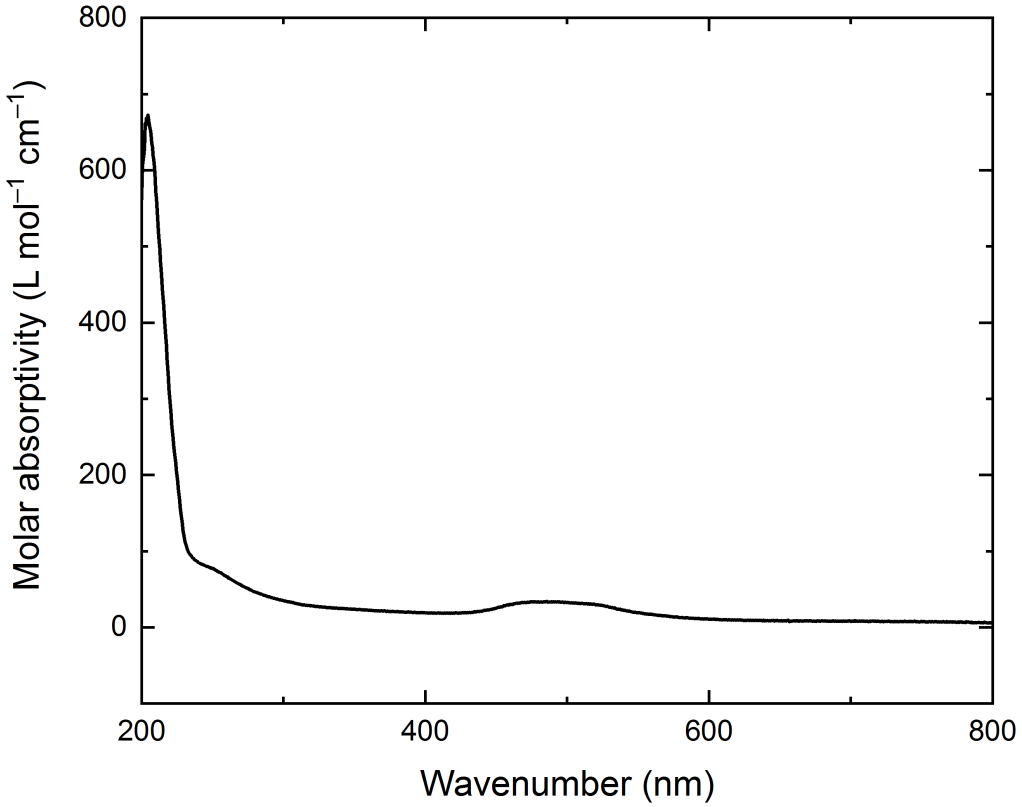

Figure S7. UV-Vis Spectra of $[Co(MeCN)_6]^{2+}$. UV-Visible spectra of the prepared complex $[Co(MeCN)_6]^{2+}$ in MeCN, exhibiting a broad manifold of absorption over the 450-550 nm range.

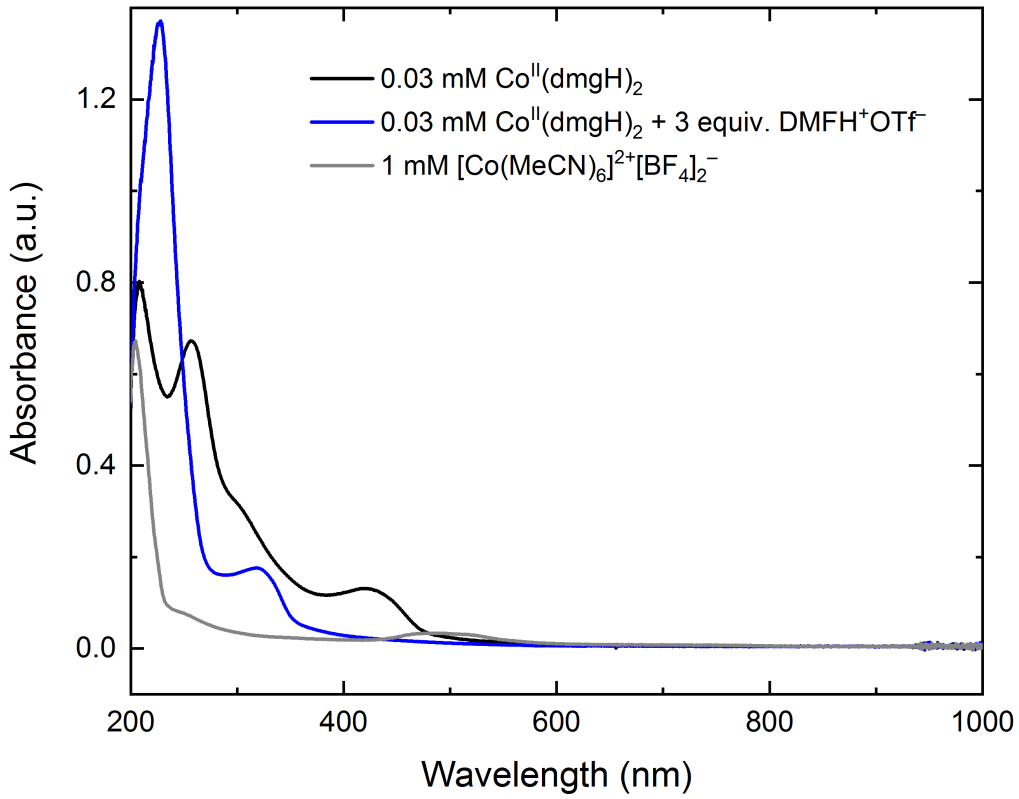

Figure S8. UV-Vis spectra of Co(dmgH)$_2$ treated with DMFH$^+$. UV-visible spectra of: the complex Co(dmgH)$_2$ (black), Co(dmgH)$_2$ treated with three equivalents of DMFH$^+$ (blue) and the complex [Co(MeCN)$_6$]$^{2+}$ (gray) in MeCN. Treatment of the cobaloxime with strong acid results in complete loss of the initial absorption features and generation of a new feature that is not associated with free ligand or the solvento cobalt complex.

NMR Spectroscopy

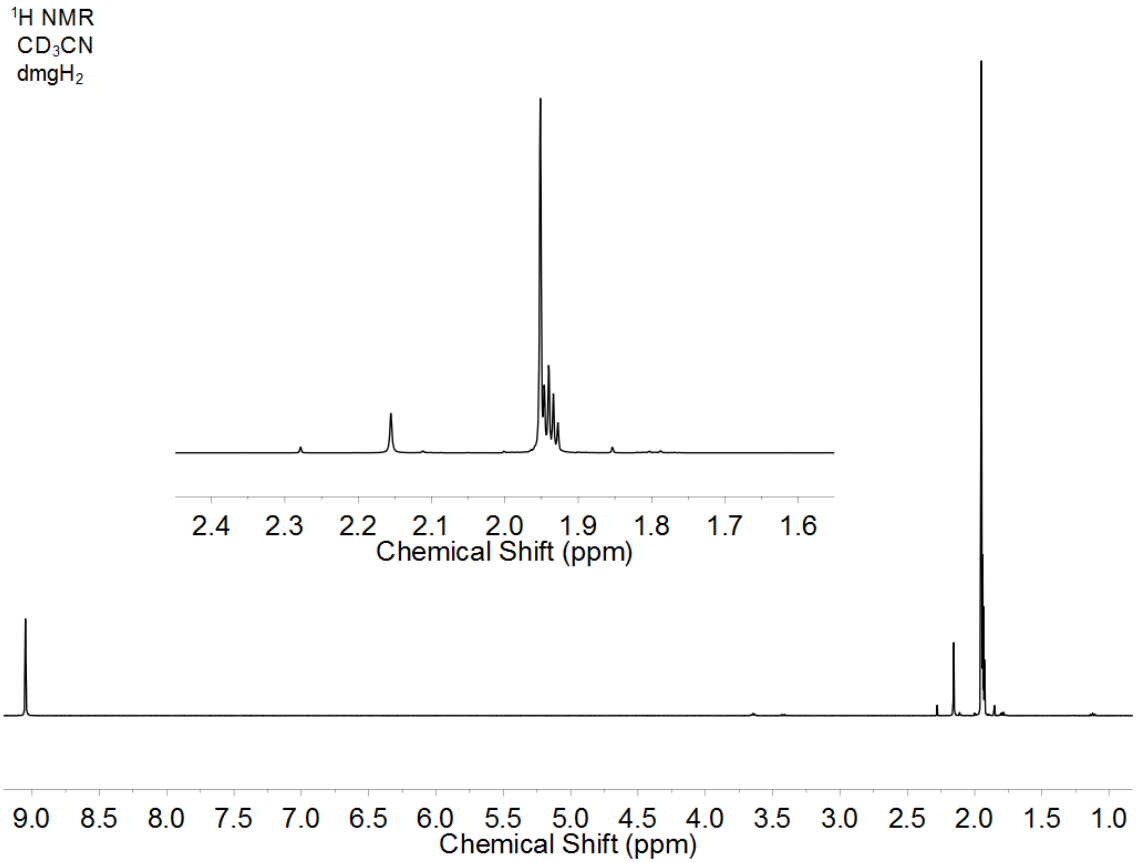

Figure S9. ^{1}H NMR spectrum of the free ligand $dmgH_2$. Spectrum of the free ligand dissolved in CD_3CN shows the signal for the equivalent methyl groups at 1.95 ppm, overlapping with the solvent residaul signal, and a singlet at 9.08 ppm corresponding the oxime protons at either end of the ligand.

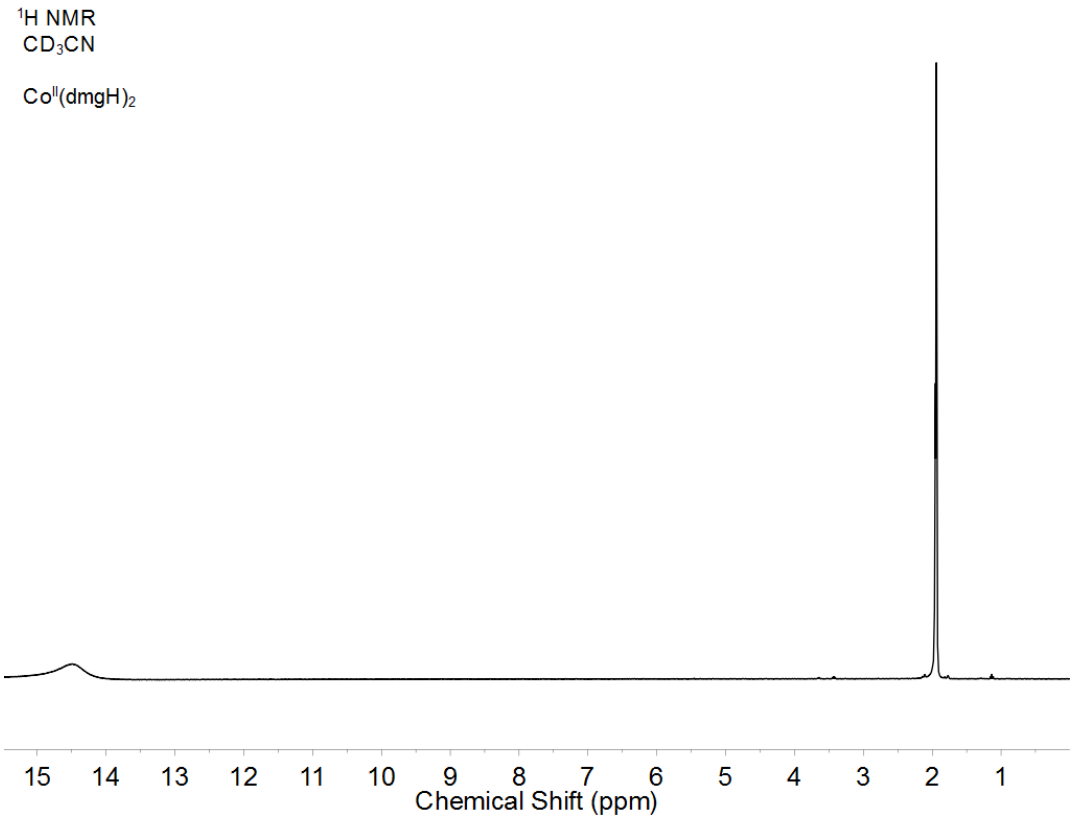

Figure S10. ^{1}H NMR Spectrum of the complex Co(dmgH)$_2$. Taken in CD_3CN, the spectrum shows that the paramagnetic Co(II) complex exhibits no visible signals in ^{1}H NMR save for the single at ca. 14.5 ppm, attributable to the bridging protons of the assembled macrocylic ligand system.

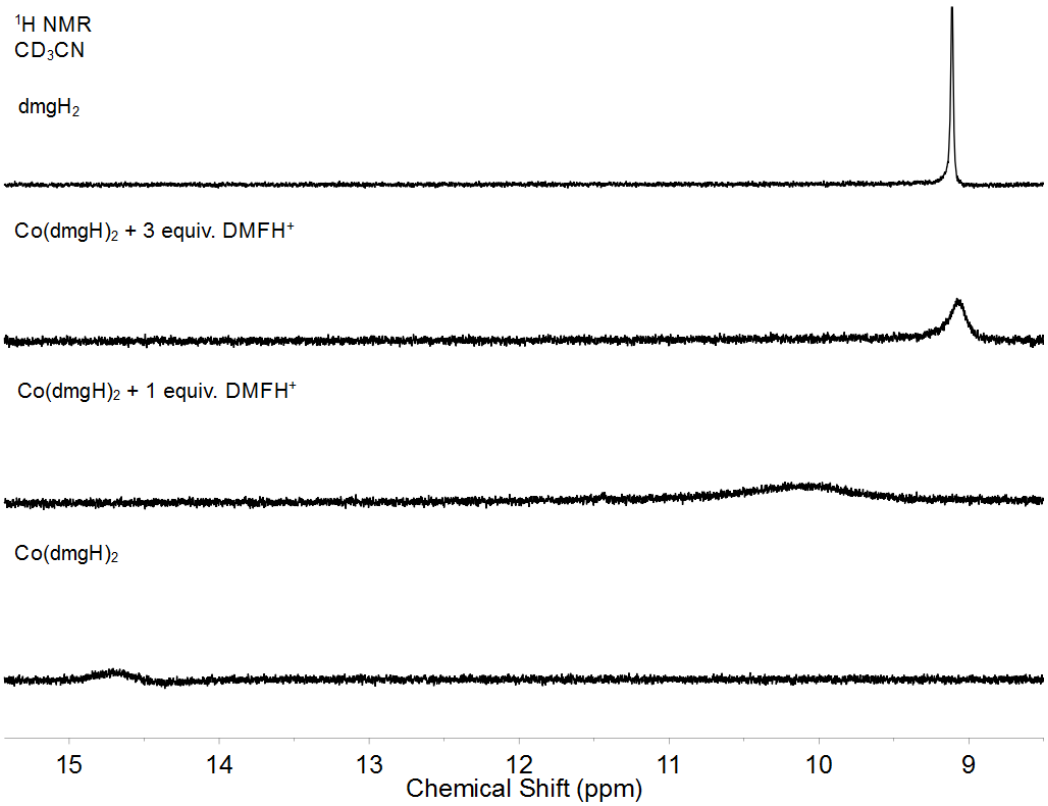

Figure S11. ^{1}H NMR Spectra of the complex $Co(dmgH)_2$ treated with $DMFH^+$. Taken in CD_3CN, the spectra show the convergence of the broad signal associated with the bridging protons in the parent complex $Co(dmgH)_2$ with a signal resembling that of free ligand following treatment of the complex with the strong acid $DMFH^+$. The signal may be broadened by the presence of paramagnetic Co(II) still present in solution.

Electrochemistry and EQCM

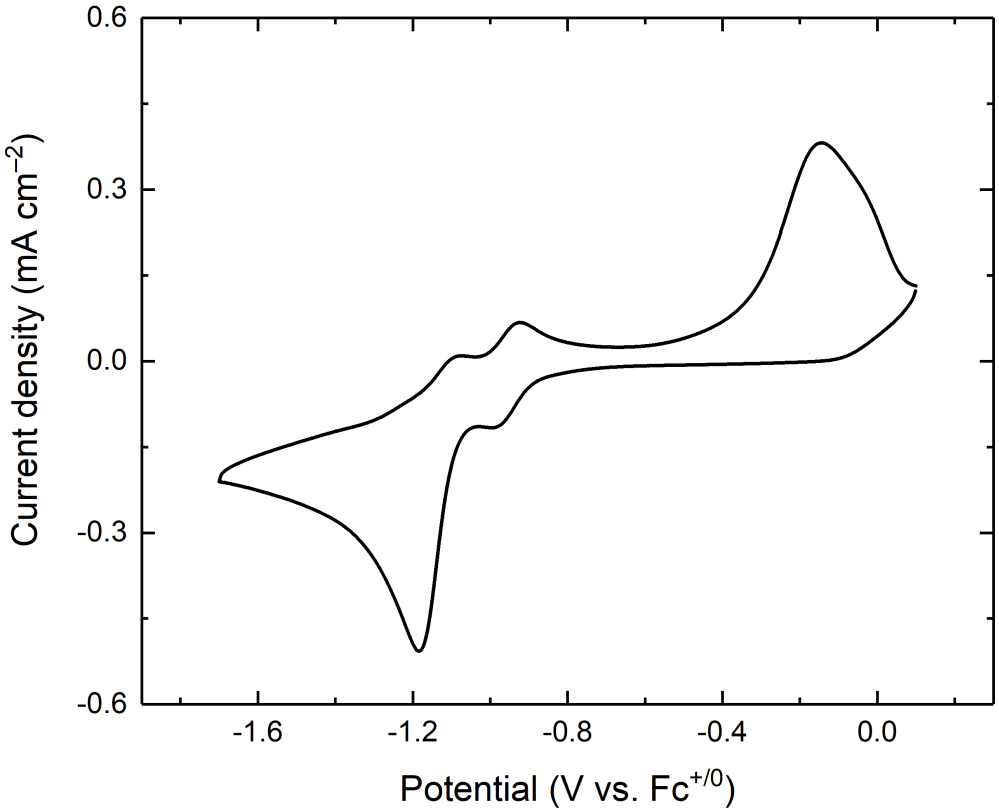

Fig S12. Electrochemistry of $Co(dmgBF_2)_2$ prepared in MeCN. Cyclic voltammogram of $Co(dmgBF_2)_2$ prepared in MeCN (as opposed to Et_2O). The quasi-reversible Co(II/I) couple is still evident centered at ca. –0.9 V vs. $Fc^{+/0}$, though the peak currents are diminished relative to a pure sample. Moreover, there is an irreversible reduction near –1.2 V which can be assigned as the reduction of $[Co(MeCN)_6]^{2+}$, generated through decomposition of the starting material with evolved HF during prior synthesis. Paired with this is a re-oxidation at more positive potentials, consistent with a surface-bound species is undergoing oxidation. In this case, this process can be assigned as anodic stripping of metallic cobalt. Conditions: ca. 1 mM [Co], 0.1 M $TBAPF_6$, HOPG working electrode, Pt counter electrode, $Ag^{+/0}$ reference electrode. Scan rate: 100 mV/s.

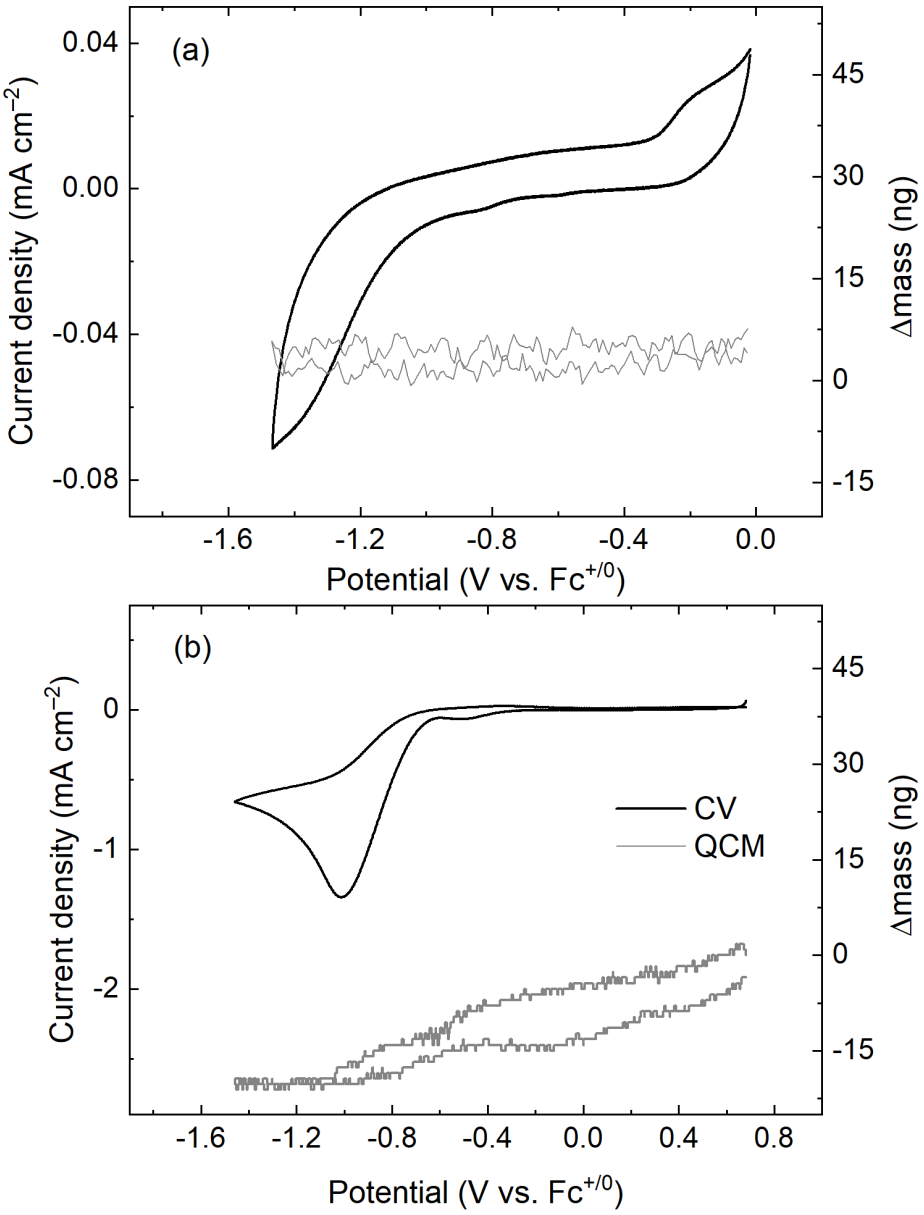

Figure S13. EQCM data for the gold electrodes. Control experiments show little change in the mass profile of the gold electrode as a function of applied potential. Here, the potential has been swept across the range of interest used in experiments with $Co(dmgH)_2$, and the voltammetry (black) shows minor reductive features in the blank at –0.5 V, –0.8 V and –1.2 V (panel a). In panel b, higher background currents are observed near –1.0 V in the presence of $DMFH^+$. However, the mass profile (gray) measured by the EQCM shows no little change in electrode mass over the potential range of interest. Conditions: 0.1 M $TBAPF_6$, Au EQCM disk working electrode, Pt counter electrode, $Ag^{+/0}$ reference electrode. Scan rate: 100 mV/s. 6 mM $DMFH^+$ included in the cell for collection of the data in panel b.

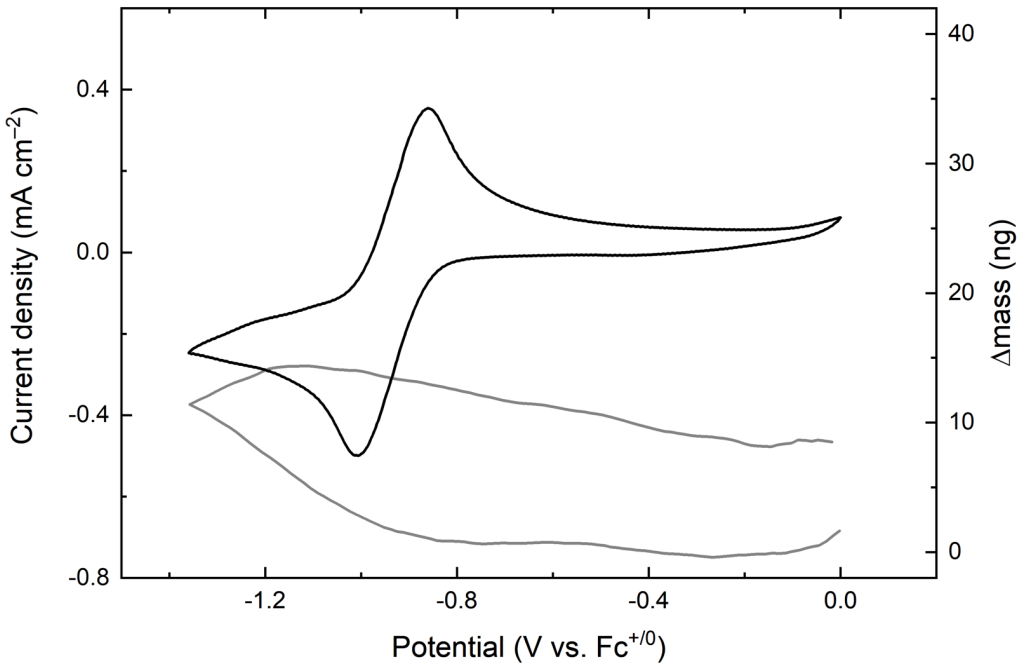

Figure S14. EQCM data for the complex Co(dmgBF$_2$)$_2$. Control experiment investigating the electrode surface behavior of the complex in the absence of acid. Voltammetry (black) shows the quasi-reversible Co(II/I) couple, and the mass profile (gray) of the system is mostly invariant as a function of applied potential. Conditions: 2 mM [Co], 0.1 M TBAPF$_6$, Au EQCM disk working electrode, Pt counter electrode, Ag$^{+/0}$ reference electrode. Scan rate: 100 mV/s.

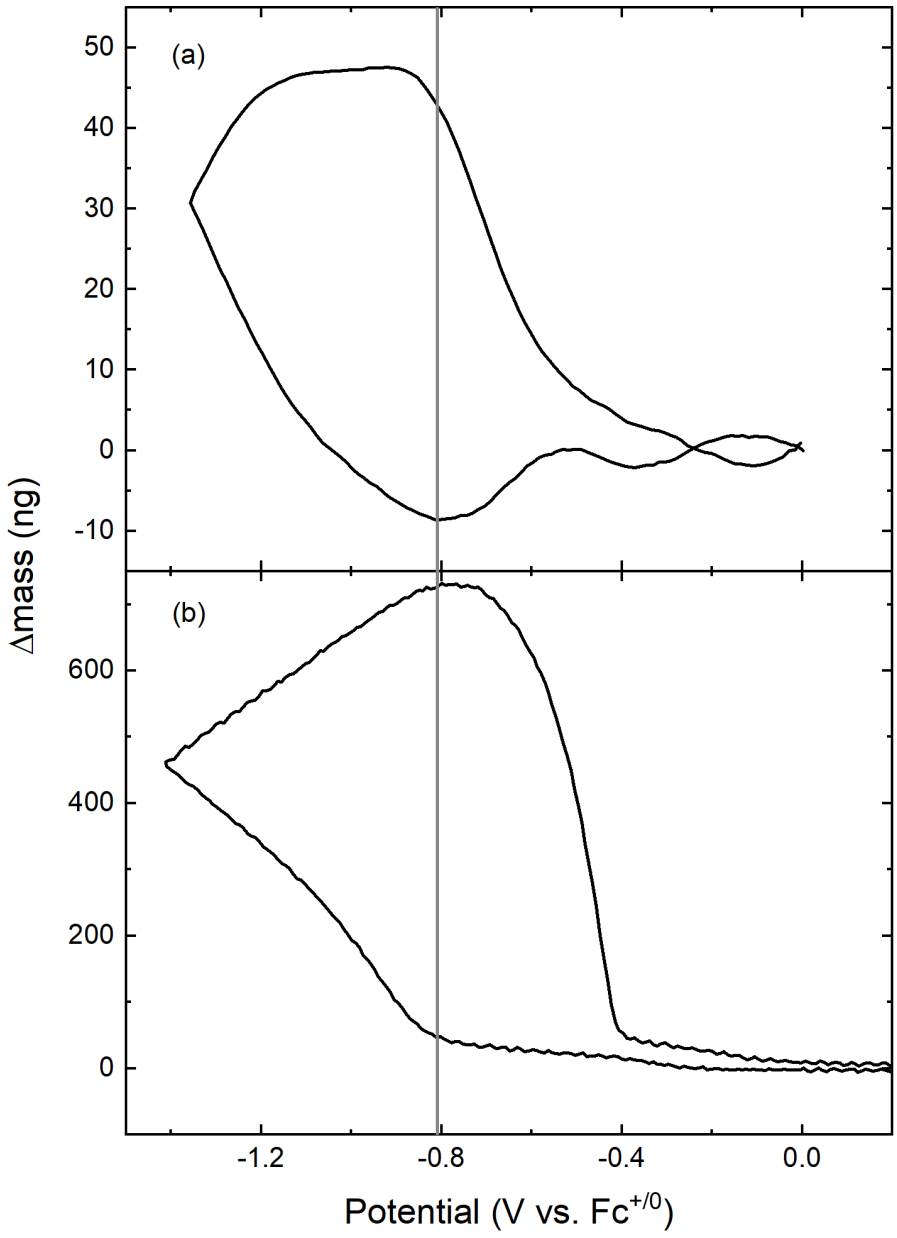

Figure S15. Onset of mass deposition for $Co(dmgBF_2)_2$ and $[Co(MeCN)_6]^{2+}$. Mass profile of both the catalyst system $Co(dmgBF_2)_2$ (panel a) and the solvento complex $[Co(MeCN)_6]^{2+}$ (panel b) as a function of applied potential. The gray line indicates the point at which onset of mass deposition begins, and is nearly identical for the two systems, suggesting mass deposition occurs through a common intermediate. Conditions: 2 mM [Co], 0.1 M $TBAPF_6$, Au EQCM disk working electrode, Pt counter electrode, $Ag^{+/0}$ reference electrode. Scan rate: 100 mV/s.

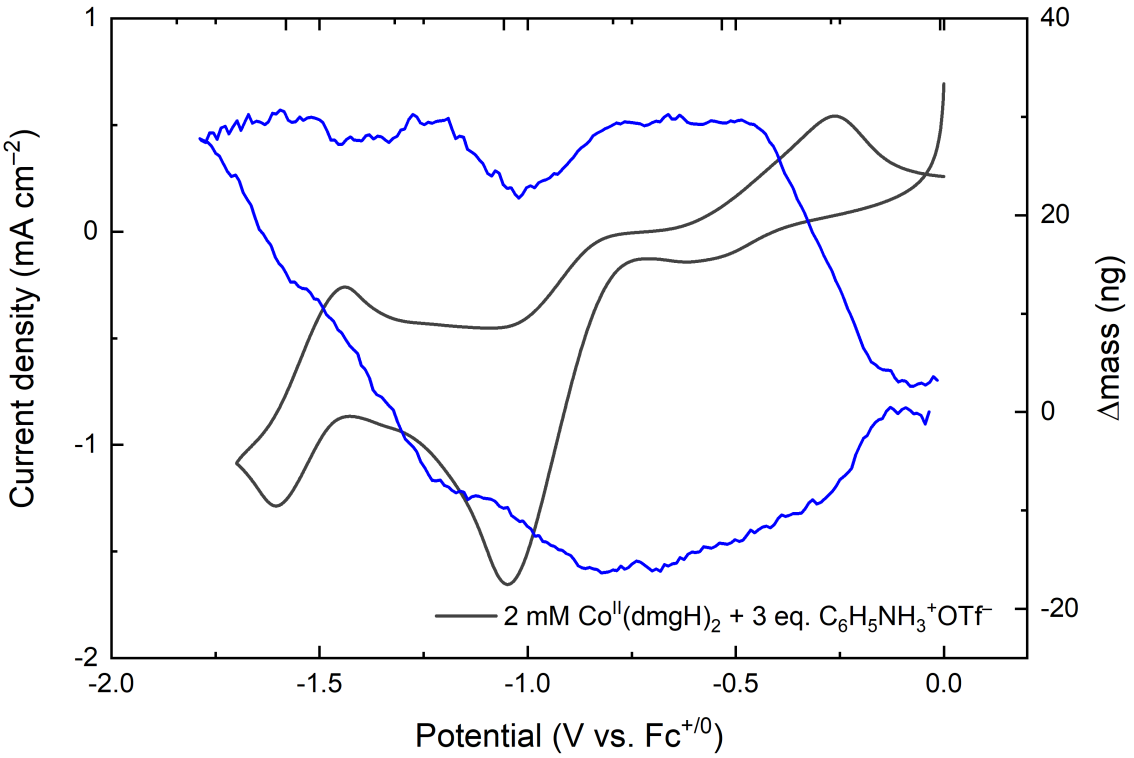

Figure S16. EQCM data for the complex $Co^{II}(dmgH)_2$ treated with $C_6H_5NH_3^+$. EQCM experiments with voltammetry (black) and mass data (blue) for $Co(dmgH)_2$ treated with three equivalents of anilinium triflate. The response qualitatively resembles the results associated with treatment of the complex with $DMFH^+$ as described in the main text. Conditions: 2 mM [Co], 0.1 M $TBAPF_6$, Au EQCM disk working electrode, Pt counter electrode, $Ag^{+/0}$ reference electrode. Scan rate: 100 mV/s.

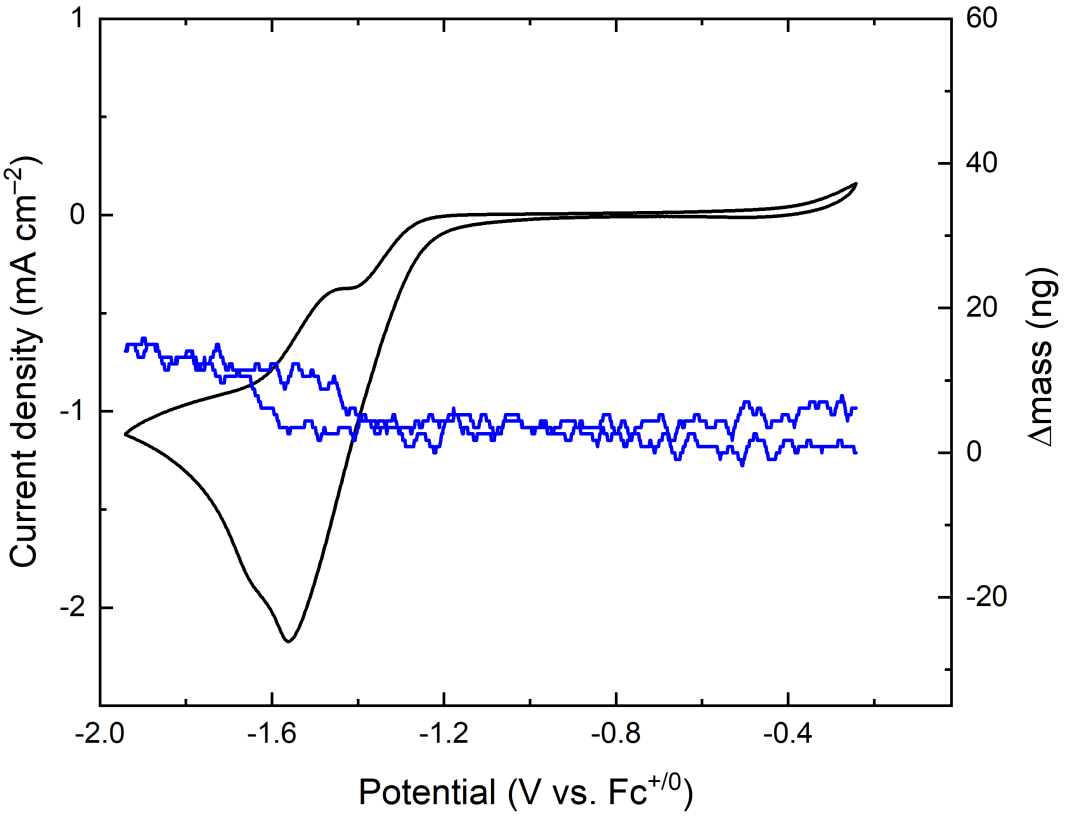

Figure S17. EQCM data for the complex $Co^{II}(dmgH)_2$ treated with Et_3NH^+. EQCM experiments with voltammetry (black) and mass data (blue) for $Co(dmgH)_2$ treated with three equivalents of triethylammonium triflate. Catalysis is observed at the potential of the cobaloxime Co(II/I) redox couple. Contrasting with the case of treatment with stronger acids, there is no observable deposition of mass at –0.8 V, suggesting that triethylammonium is too weak to destructively protonate the precatalyst. Similarly, there is no anodic stripping feature in the voltammetry. Conditions: 2 mM [Co], 0.1 M $TBAPF_6$, Au EQCM disk working electrode, Pt counter electrode, $Ag^{+/0}$ reference electrode. Scan rate: 100 mV/s.

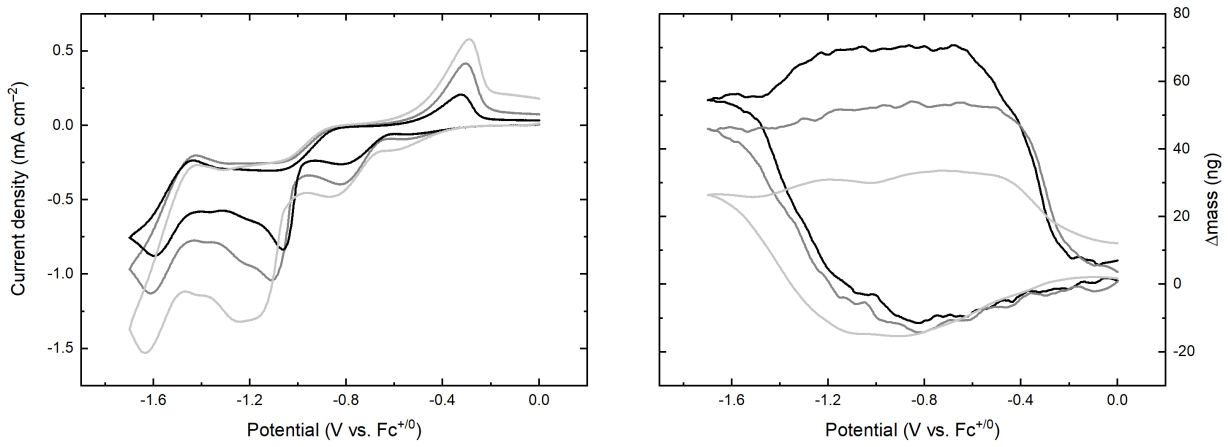

Figure S18. Scan rate dependence of EQCM results with $Co^{II}(dmgH)_2$. Voltammetry (left panel) and mass data (right panel) for $Co(dmgH)_2$ treated with 3 equiv. $DMFH^+$. Scan rate increases from dark to light (black: 50 mV/s, dark gray: 100 mV/s, light gray: 200 mV/s). As scan rate increases, observed current increases but total mass deposited is diminished. This is consistent with the lesser amount of time that the electrode remains at sufficiently negative potentials to drive deposition of heterogeneous material. Note that the behavior of the system remains qualitatively similar at the various scan rates, with a period of plateauing mass change that remains until the onset of oxidative stripping at more positive potentials. Conditions: 2 mM [Co], 6 mM $DMFH^+$, 0.1 M $TBAPF_6$, Au EQCM disk working electrode, Pt counter electrode, $Ag^{+/0}$ reference electrode. Scan rate: 100 mV/s.

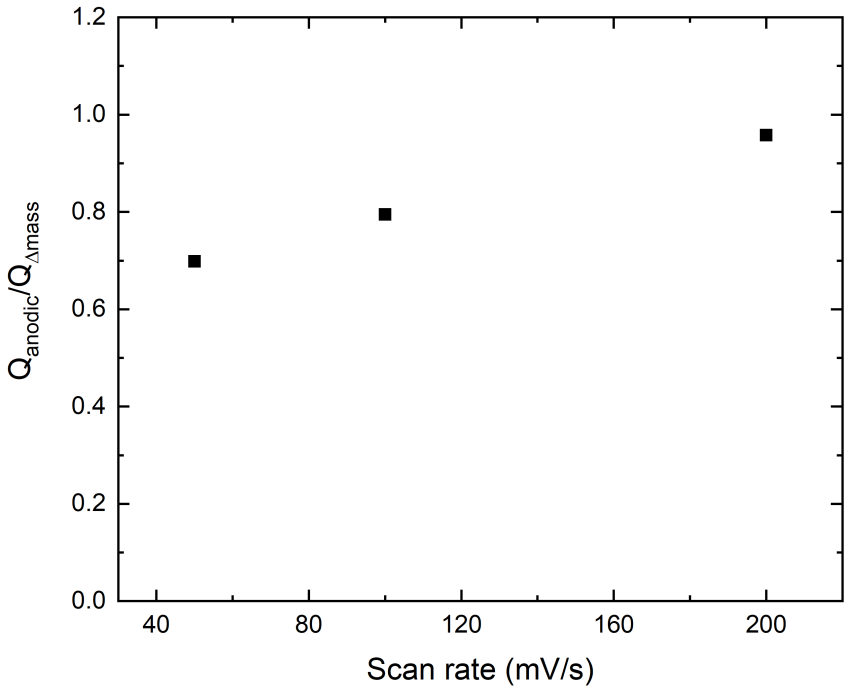

Figure S19. Efficiency of oxidative stripping as a function of scan rate. Calculated efficiency of oxidative stripping from scan rate-dependent EQCM data on $Co(dmgH)_2$ treated with three equivalents of $DMFH^+$ (see Figure S18). The charge equivalent of mass stripped (Q_{anodic}, determined by integration of the anodic stripping wave to determine charge and thus predicted mass of cobalt) was divided by the charge equivalent of the total actual mass lost ($Q_{\Delta mass}$, measured by the EQCM and assuming $2e^-$ passed per Co^0 equivalent) and plotted as a function of scan rate. In agreement with the observation that chemical corrosion is slow under the conditions at the electrode during voltammetry, slower scan rates result in lower 'efficiency' of oxidative stripping (i.e., a larger contribution of chemical corrosion by acid) as the solid cobalt material is allowed more time at cathodically unprotected potentials to react with acid moving into the reaction-diffusion layer around the electrode.

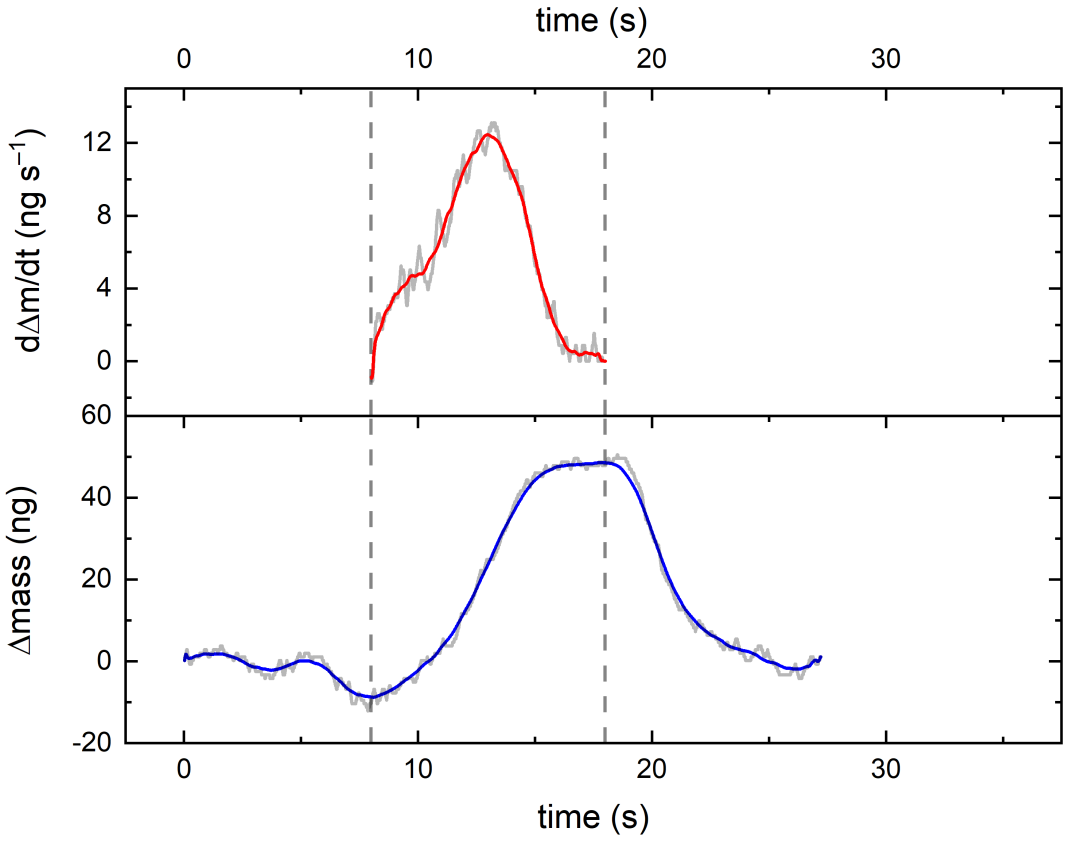

Figure S20. Derivative of mass deposition data for $Co^{II}(dmgBF_2)_2$. Plot of the mass-versus-time data (lower panel; gray line raw data, blue line smoothed 100 pt. adjacent averaging) and associated derivative plot (upper panel; gray line raw data, red line smoothed 45 pt. adjacent averaging) from an EQCM experiment carried out with the BF_2-bridged cobaloxime (see main text, Figure 4b).

The derivative of the region denoted by the gray dashed vertical lines was calculated to generate the data in the upper panel; the derivative plot shows that there is an acceleration in mass deposition followed by a deceleration of mass deposition rate.

Conditions: working electrode, Au EQCM disk; scan rate, 100 mV/s. Estimated error is ±5 ng.

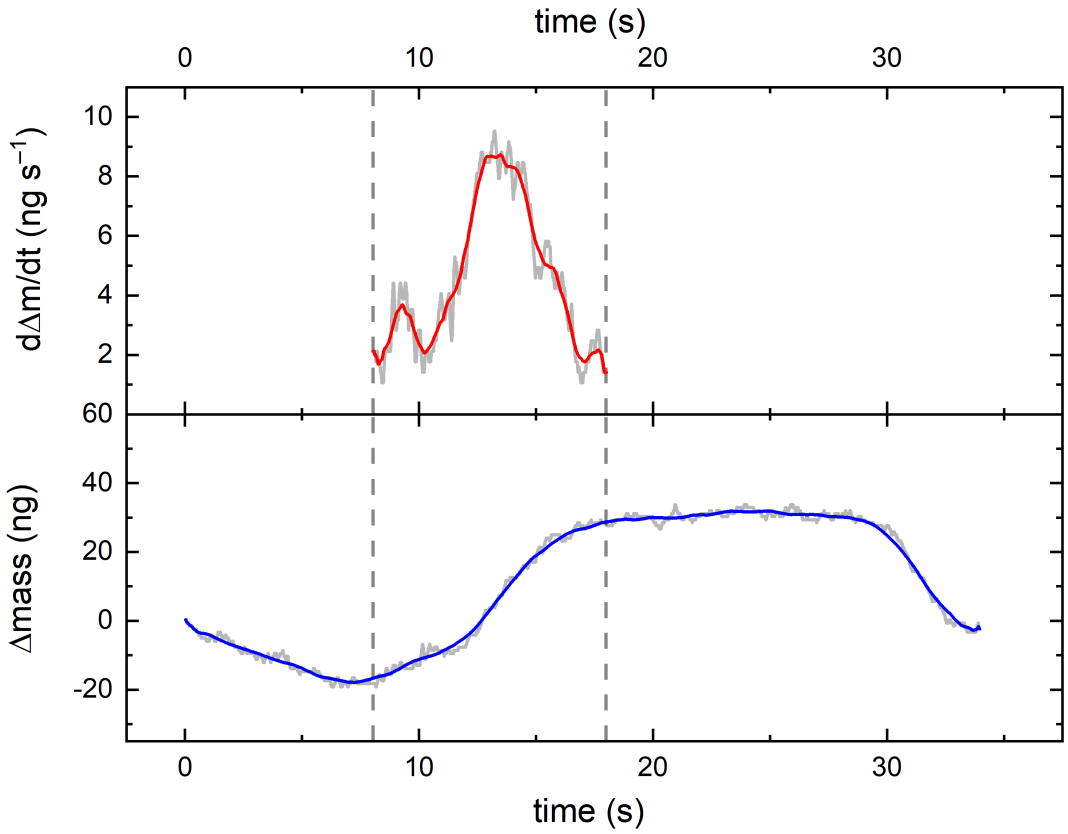

Figure S21. Derivative of mass deposition data for $Co^{II}(dmgH)_2$. Plot of the mass-versus-time data (lower panel; gray line raw data, blue line smoothed 100 pt. adjacent averaging) and associated derivative plot (upper panel; gray line raw data, red line smoothed 45 pt. adjacent averaging) from an EQCM experiment carried out with the H^+-bridged cobaloxime (see main text, Figure 4a).

The derivative of the region denoted by the gray dashed vertical lines was calculated to generate the data in the upper panel; the derivative plot shows that there is an acceleration in mass deposition followed by a deceleration of mass deposition rate.

Conditions: working electrode, Au EQCM disk; scan rate, 100 mV/s. Estimated error is ±5 ng.

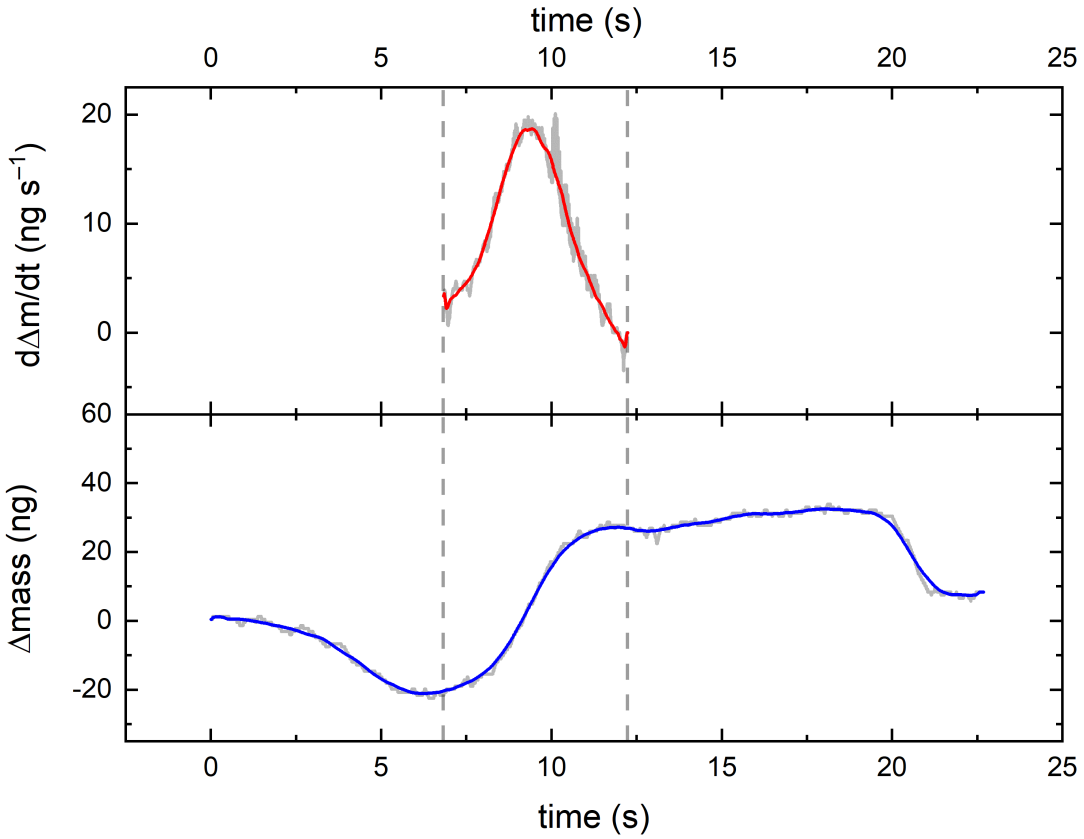

Figure S22. Derivative of mass deposition data for $Co^{II}(dmgH)_2$ at higher scan rate. Plot of the mass-versus-time data (lower panel; gray line raw data, blue line smoothed 100 pt. adjacent averaging) and associated derivative plot (upper panel; gray line raw data, red line smoothed 45 pt. adjacent averaging) from an EQCM experiment carried out with the H^+-bridged cobaloxime at 150 mV/s.

The derivative of the region denoted by the gray dashed vertical lines was calculated to generate the data in the upper panel; the derivative plot shows that there is an acceleration in mass deposition followed by a deceleration of mass deposition rate.

Conditions: working electrode, Au EQCM disk; scan rate, 150 mV/s. Estimated error is ±5 ng.